

# A Closer Look at the Dynamical State of the High-redshift Galaxy Cluster SPT-CL J2215-3537

VINICIUS S. BESSA ,<sup>1</sup> RENATO A. DUPKE ,<sup>1,2</sup> AND YOLANDA JIMÉNEZ-TEJA ,<sup>3,1</sup><sup>1</sup>*Observatório Nacional, Rua General José Cristino, 77, Bairro Imperial de São Cristovão Rio de Janeiro, RJ 20921400, Brazil*<sup>2</sup>*Department of Astronomy, University of Michigan, 311 West Hall, 1085 South University Ave., Ann Arbor, MI 48109-1107*<sup>3</sup>*Instituto de Astrofísica de Andalucía-CSIC, Glorieta de la Astronomía s/n, E-18008 Granada, Spain*

## ABSTRACT

We present a comprehensive reanalysis of the dynamical state of the high-redshift galaxy cluster SPT-CL J2215-3537 ( $z = 1.16$ ), using the full set of available Chandra observations to characterize the thermodynamic and morphological properties of the intracluster medium. Although previously identified as one of the most distant dynamically relaxed systems based on X-ray morphological statistics, we find compelling evidence that SPT-CL J2215-3537 displays some level of dynamical activity. This includes temperature anisotropies consistent with the first detection of a pair of core-sloshing cold fronts at  $z > 1$ . We identify a ghost cavity candidate and estimate its mechanical power as  $\log_{10}(P_{\text{cav}}/10^{42} \text{erg s}^{-1}) = 2.66 \pm 0.23$ , confirming that radiative cooling strongly exceeds active galactic nucleus feedback heating. We show that SPT-CL J2215-3537 is likely in a short transient phase preceding the onset of a self-regulated cooling-feedback cycle. We recalculate traditional X-ray morphological parameters and discuss how non-self-similar evolution of parameters sensitive to the surface brightness cuspiness can bias dynamical classifications at high redshift.

**Keywords:** Galaxies: clusters: individual: SPT-CL J2215-3537 – Galaxies: clusters: intracluster medium – X-rays: galaxies: clusters

## 1. INTRODUCTION

As the most recently formed gravitationally bound objects in the Universe, galaxy clusters represent a unique laboratory for probing the nonlinear regime of large-scale structure formation, providing precise constraints on the underlying cosmological model. For instance, the abundance of clusters as a function of their mass,  $dN/dM$ , is sensitive to the matter density,  $\Omega_m$ , and to the amplitude of matter fluctuations on a scale of  $8 h^{-1} \text{Mpc}$ ,  $\sigma_8$  (Press & Schechter 1974; Bahcall & Cen 1993). The distribution of clusters in redshift space,  $dN/dz$ , carries information on the dark energy equation-of-state parameter,  $w_0$ , through its dependence on the growth factor,  $D_z$  and the cosmological volume element  $dV/dz$  (Haiman et al. 2001). Furthermore, due to the dominance of gravitational effects, it is expected that the gas mass fraction,  $f_{\text{gas}} = M_{\text{gas}}/M_{\text{tot}}$ , in massive virialized clusters  $\gtrsim r_{2500}$  resembles the cosmic baryon fraction,  $\Omega_b/\Omega_m$  (White et al. 1993; Sasaki 1996; Allen et al. 2002), and that, in this regime, it is fairly independent of redshift and halo mass (Angelini et al. 2023; Popesso et al. 2024). The  $f_{\text{gas}}$  method has been used, in combination with external priors, to place

constraints on  $\Omega_m$ ,  $\Omega_\Lambda$ , and  $w$  (Allen et al. 2002; Ettori et al. 2009; Mantz et al. 2014, 2022), providing independent evidence for cosmic acceleration.

The primary limitation of cluster counts and the  $f_{\text{gas}}$  method as cosmological probes is the accurate determination of cluster masses. Generally, estimating the total halo mass requires the use of observable proxies, such as the X-ray emission from the intracluster medium (ICM), the weak lensing (WL) shear, or the Sunyaev-Zel'dovich (SZ) effect signal. The X-ray-derived mass typically relies on the assumptions of spherical symmetry and hydrostatic equilibrium (HSE) between the thermal gas and the gravitational potential, introducing a bias due to non-thermal pressure support from bulk motions, active galactic nuclei (AGN) feedback and turbulence, which can underestimate the total mass by tens of percent depending on the dynamical state of the gravitating material (Nagai et al. 2007; Lau et al. 2009). Many studies indicate that the hydrostatic mass bias is significantly reduced for derived masses at  $r_{2500}$  (Evrard et al. 1996; Rasia et al. 2006; Mahdavi et al. 2008). Moreover, several analytical corrections and calibrations have been proposed to systematically ac-

count for non-thermal components and recover true halo masses (e.g., Rasia et al. 2004; Nelson et al. 2012; von der Linden et al. 2014; Applegate et al. 2016). However, this scenario becomes significantly more complex for dynamically active systems (e.g., those experiencing recent or ongoing merger events). Nelson et al. (2014) demonstrated through the analysis of 62 clusters from a high-resolution cosmological simulation that the hydrostatic bias in current/post-merger clusters can vary strongly with radius, becoming either highly positive or negative depending on the position of the infalling structure and making general mass correction schemes impractical. Additionally, an irreducible bias arises from gas acceleration components, which becomes non-negligible in unrelaxed systems, particularly in the high-redshift regime where mergers are more frequent. Even though the WL method is generally considered to be independent of dynamical assumptions, since its signal is proportional to the projected potential of the system, breaking the mass-sheet degeneracy still requires the adoption of a density analytical profile, which can be unsuitable for merging clusters (Lee et al. 2023). Additionally, the SZ-derived masses also inherit dependence on the cluster’s dynamical state through their calibration with X-ray observables. One can avoid the strong dependence on the dynamical state by using the caustic technique to estimate the cluster’s mass profile from kinematic information out to beyond  $R_{200}$  (Diaferio & Geller 1997; Diaferio 1999; Maughan et al. 2016). However, in order to estimate the escape velocity profile, one needs a sufficiently high number of member galaxy redshifts, with at least  $\sim 100$  well constrained redshifts in the outskirts (Diaferio 2009), which limits the applicability of the method for fainter targets.

Therefore, precise dynamical state classification is critical for cosmological applications, as mostly relaxed clusters provide sufficiently unbiased halo mass estimates. In the absence of high-quality spectroscopic data, the dynamical state of clusters may be inferred from the morphological regularity of the ICM X-ray emission. The pioneering work of Allen et al. (2002), which established some of the first cosmological constraints from  $f_{\text{gas}}$  measurements, selected relatively relaxed systems based on the sharpness of X-ray surface brightness peaks, isophote shapes, and isophote centroid variations, in addition to optical morphologies and gravitational lensing data, when available. Further studies (Allen et al. 2004, 2008) extended the samples to X-ray luminous clusters in the redshift range  $\sim 0.05 < z < \sim 1$ , refining the selection criteria to include central cooling times and several other proxies for high-redshift sys-

tems with intermediate features. Many other works employed X-ray morphological parameters to trace substructures/inhomogeneities in galaxy clusters (Jeltema et al. 2005; Hashimoto et al. 2007; Parekh et al. 2015; Zenteno et al. 2020; Yuan & Han 2020). This is a natural step, since the morphology parameters are directly calculated from the X-ray imaging, without requiring spectral modeling to derive the physical properties of the ICM. This allows for an automated approach to classify the increasing number of intermediate and high-redshift clusters currently detected via SZ and X-ray techniques prior to the upcoming powerful spectro-imagers such as AXIS (<https://axis.umd.edu/>) (Russell et al. 2024) and NewAthena (<https://www.cosmos.esa.int/web/athena>) in the next decade, and also by the current large scale surveys such as J-PAS ([www.j-pas.org/](http://www.j-pas.org/)) and LSST ([www.lsst.org/](http://www.lsst.org/)).

Building upon this scheme, Mantz et al. (2015) developed the Symmetry–Peakiness–Alignment (SPA) criteria, a set of X-ray morphological parameters, designed to be applicable to large datasets spanning a wide range of redshifts, masses, and data qualities. With this framework, Mantz et al. (2022) included the high-redshift ( $z = 1.16$ ) cluster SPT-CL J2215-3537 (SPT2215 hereafter) (Bleem et al. 2020) in their extended sample of massive relaxed clusters suitable for  $f_{\text{gas}}$  cosmology. Calzadilla et al. (2023) identified it as the most distant relaxed cool core cluster at the time, providing evidence for a highly efficient central cooling and a remarkably high star formation rate in the brightest cluster galaxy (BCG). However, recent studies have been reevaluating, using independent methods, the dynamical state of galaxy clusters previously classified as relaxed based on morphological parameters. For instance, Jiménez-Teja et al. (2023) performed a multiwavelength study of the high-redshift ( $z = 0.97$ ) cluster SPT-CLJ0615-5746, which was also one of the objects included in the extended sample of massive relaxed clusters, aiming to probe the dynamical state of the system through the intracluster light fraction ( $f_{\text{ICL}}$ ) and the X-ray emission of the ICM. The work found a distribution of rest-frame  $f_{\text{ICL}}$  inconsistent with a relaxed system. Additionally, the temperature map derived from the X-ray analysis showed signatures of multiple mergers.

In this work, we re-examine the dynamical state of SPT2215 with newly released Chandra data and discuss the effectiveness of morphological parameters as cluster relaxation proxies, particularly at high redshift. The paper is organized as follows. In Section 2, we describe the X-ray data reduction and perform a spectral analysis

to derive thermodynamic profiles and maps. In Section 3, we analyze the merged X-ray image to characterize the spatial properties of the ICM gas, additionally computing commonly used morphological parameters. Section 4 discusses the results of our combined analysis and proposes consistent scenarios for SPT2215’s dynamical history. Finally, Section 5 summarizes our findings and present future research directions based on our conclusions.

## 2. X-RAY SPECTRAL ANALYSIS

All relevant quantities were calculated considering a standard flat  $\Lambda$  cold dark matter cosmology, with  $H_0 = 70 \text{ km s}^{-1} \text{Mpc}^{-1}$ ,  $\Omega_m = 0.3$ , and  $\Omega_\Lambda = 0.7$ . Unless otherwise noted, all quoted uncertainties represent  $1\sigma$  confidence intervals and, when needed, are propagated using the partial derivatives method considering the covariance matrices given by the fits. The science products were obtained in the usual way using the X-ray Data Analysis Software (CIAO 4.17, Fruscione et al. 2006). We used all ten archived Chandra observations available: three were taken with ACIS-I (OBS-ID: 22653, 24614, 24615; PI: McDonald), and seven with ACIS-S (OBS-ID: 25468, 25902, 25903, 25904, 26244, 26372, 27614; PI: Mantz). The individual observations were downloaded and reprocessed using up-to-date calibration data from CALDB version 4.11.6 with additional background cleaning for the VFAINT telemetry mode. The reprocessed events files were filtered to the 0.5–7 keV band and the ACIS-I3 or ACIS-S3 chips were selected according to the observation. The exposure maps were created with the *fluximage* script using source characteristic spectral weights. Point sources were removed using the *wavedetect* tool followed by an additional eye check. Bad time intervals were identified through the source lightcurves in order to eliminate flares and create cleaned event files. The total filtered exposure time was 188.12 ks.

### 2.1. Radial Thermodynamic Profiles

Annuli regions around the BCG position ( $\alpha = 22^{\text{h}}15^{\text{m}}03^{\text{s}}9306$ ,  $\delta = -35^\circ 37' 17.''885$ ) were selected. The correspondent Blank-Sky files were used to account for the background contribution. The spectra of all reprojected observations were extracted using *specextract* and then simultaneously fitted with a *phabs\*apc* model using Xspec version 12.14.1 (Arnaud 1996). The abundances were fixed at  $0.3 Z_\odot$ , where  $Z_\odot$  is the solar photospheric elemental abundance of Anders & Grevesse (1989). Temperatures were tied to each other and the remaining parameters were kept independent. The hydrogen column was fixed at  $nH = 1.01 \cdot 10^{20} \text{ cm}^{-2}$

according to the HI4PI survey (HI4PI Collaboration et al. 2016). The deprojection of thermodynamic quantities was performed using the onion-peeling method under the assumption of spherical symmetry in concentric shells, similarly to the recipe presented in Ghizzardi et al. (2004). The electron number density  $n_e$  was derived from the deprojected normalization parameter  $N$  of the spectral model,

$$n_e = 10^7 D_A (1+z) \sqrt{\frac{4\pi N}{0.83V}}, \quad (1)$$

where  $D_A = 1701.686$  Mpc is the angular diameter distance,  $z = 1.16$  is the redshift,  $V$  is the considered shell volume, and 0.83 term comes from the factor between the proton density and the electron density ( $n_p = 0.83n_e$ ). We additionally fit the surface brightness with a one-dimensional beta model, assuming the cooling function  $\Lambda(k_B T, Z)$  parameterized by Tozzi & Norman (2001), allowing us to obtain an analytical curve for the electron number density, given by

$$n_e(r) = n_0 \left[ 1 + \left( \frac{r}{r_c} \right)^2 \right]^{-3\beta/2}. \quad (2)$$

The core radius  $r_c$ , the beta parameter  $\beta$  and the central surface brightness  $S_0$  come directly from the fit. The central density is calculated using the following.

$$n_0 = \left[ \frac{S_0}{\sqrt{\pi} r_c \Lambda(k_B T, Z)} \frac{\Gamma(3\beta)}{\Gamma(3\beta - 0.5)} \right]^{1/2}, \quad (3)$$

where  $\Gamma(x)$  represents the gamma function. With the temperature  $T$  and the electron number density  $n_e$  profiles, we can easily compute the pseudopressure and pseudoentropy, which are, respectively, given by the following relations

$$P(r) = 1.92 n_e k T, \quad (4)$$

$$K(r) = k T n_e^{-2/3}, \quad (5)$$

where  $k$  is the Boltzmann constant. Assuming a compressionless thermal cooling, we can calculate the cooling time as

$$t_c(r) = \frac{3P}{2n_e^2 \Lambda(k_B T, Z)}. \quad (6)$$

Figure 1 shows the deprojected electron density profile both from the spectral modeling and from the  $\beta$ -model fit. The electron density exhibits a pronounced decline at  $r_{\text{sharp}} = 159 \pm 5 \text{ kpc} / \sim 19.3 \pm 0.6 \text{ arcsec}$ . In Figure 2 we show the correspondent radial profiles of the main 3D thermodynamic quantities. The feature in

$r_{\text{sharp}}$  is further corroborated in the thermodynamic profiles, where we observe a steep rise in both temperature and entropy beyond the discontinuity, while the pressure remains nearly constant. All projected radial profiles consistently point toward a common feature: a contact discontinuity located at a projected radius of approximately 160 kpc. The presented picture is consistent with the physical conditions expected for a cold front. Interestingly, the estimated cooling radius,  $r_{\text{cool}} = 147 \pm 10$  kpc /  $17.8 \pm 1.2$  arcsec, defined here as the radius where the local cooling time matches the age of the Universe at the cluster's redshift ( $\sim 5.17$  Gyr), is very close to the location of the discontinuity. Another feature worth mentioning is the flat central temperature profile for regions below  $r_{\text{cool}}$ . Although SPT2215 manifest clear properties of a well developed cool core (e.g., centrally peaked surface brightness, central entropy below 30 keV·cm<sup>2</sup>, central cooling time below 1 Gyr), its temperature profile deviates from the classical cool core behavior, lacking the expected continuous decline toward the cluster center.

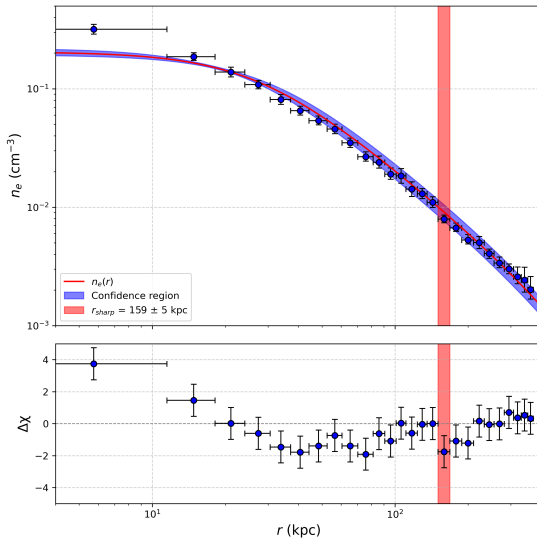


**Figure 1.** Top: Deprojected electron density profile. The blue dots were obtained from Equation 1, while the red curve corresponds to the  $\beta$ -model applied to the surface brightness profile, whose optimal parameters are inserted in Equation 2. Bottom: residual between the data and the model. The sharp decline observed in both the density profile and the residual around  $r_{\text{sharp}} \approx 160$  kpc / 19.4 arcsec is associated to two symmetric cold fronts.

As a consistency check, we verify that our temperature and emission measure profiles are equivalent to those presented by Calzadilla et al. (2023) when using the same first three observations. By using all ten observations, we obtain a mean reduction in the uncertainties

by a factor of  $\sim 2$  for both the temperature and normalization fits. This improvement allows us to choose finer radial bins (necessary to detect the discontinuity) and construct thermodynamic maps, which would not be achievable with the required statistical significance solely with the initial set of observations. The radial extent of our analysis ( $\sim 430$  kpc / 48.5 arcsec) was determined by identifying out to which radius the spectral fits no longer converge. We note that the source surface brightness becomes comparable to the background level at  $\sim 580$  kpc / 70 arcsec. Finally, we verify that the results we obtain using the rescaled blanksky files are consistent to those derived using a local background region.

## 2.2. Projected Thermodynamic Maps

In order to easily identify directions of interest and probe potential anisotropies in the physical properties of the ICM, we constructed maps of the projected thermodynamic parameters. To do so, we first applied a Weighted Voronoi Tesselations (WVT) algorithm to partition the field of view, ensuring a nearly constant S/N. The basic Voronoi Tesselations algorithm for spatial adaptive binning is described in details in Cappellari & Copin (2003). Several applications of the WVT method to X-ray data are presented in Diehl & Statler (2006), as well as its advantages over other well-used algorithms such as the Quadtree (Sanders & Fabian 2001). Then, the spectrum of each region/bin is extracted and fitted with Xspec using the *phabs\*apec* model as before. The WVT algorithm naturally minimizes the sharpness of bin edges, but they are still discontinuous. To improve the visualization, we applied Universal Kriging interpolation using the PyKriging<sup>1</sup> Python package (version 1.7.2; Murphy et al. 2024), which allows spatial smoothing while accounting for the underlying trends in the data.

In Figure 3 we present the maps of the projected thermodynamic quantities. It is important to note that because of the low S/N regime, these maps should be read qualitatively. The temperature map shows some interesting features. First, it appears that the coldest region is displaced from the BCG center by roughly 5 arcsec ( $\sim 50$  kpc) to the southeast. We fit the spectra of a joint set of these peripheral cold clumps, indicated in Figure 3 as white ellipses, and find a statistical significance of

<sup>1</sup> The package documentation is available on <http://pykrige.readthedocs.io/>. The temperature and entropy maps used a spherical variogram model with linear drift terms, while the pressure map used a hole-effect variogram model, as the standard ones were unable to adequately capture the spatial structure of the data.

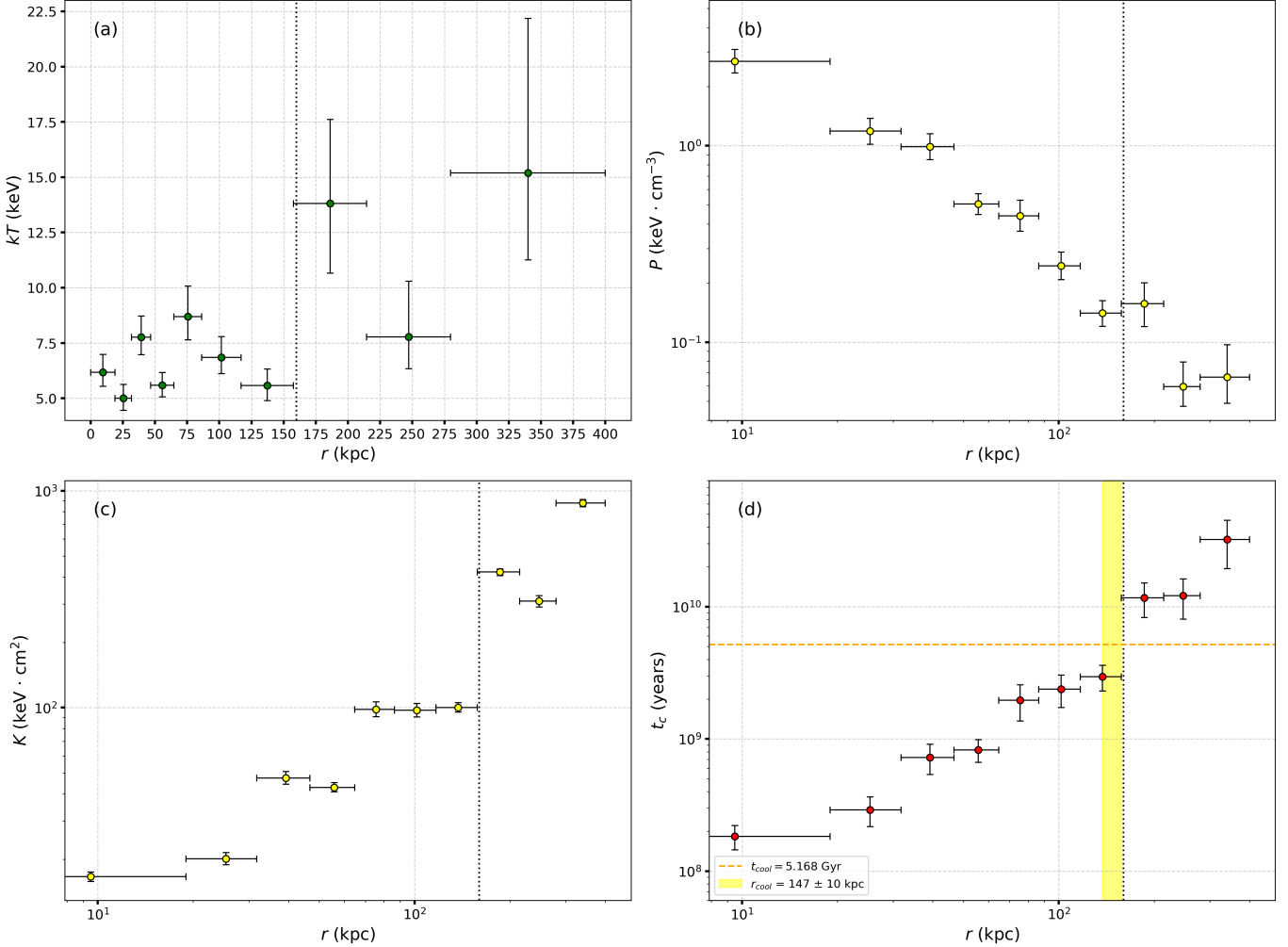


**Figure 2.** Radial profiles of various 3D thermodynamic quantities: (a) Temperature ( $kT$ ), (b) Pressure ( $P$ ), (c) Entropy ( $K$ ), and (d) Cooling Time ( $t_c$ ). The shaded region in (d) indicates the cooling radius  $r_{cool}$ . The dotted vertical line in all panels mark  $r = 160$  kpc to indicate the approximate projected radius of the observed discontinuity.

$1.8\sigma$  that these regions are indeed colder than the center. The second feature is the apparent sudden temperature increase in the southeast and northwest directions approximately around  $r_{cool}$ , confirming the orientation of the discontinuities. On the other hand, the entropy map exhibits a smoother distribution in the core, with its lowest value aligned with the cluster's center. The pressure map suggests the presence of possible central substructures, with a higher pressure tail towards the NE direction.

### 2.3. Directional Thermodynamic Profiles

Based on the spatial features revealed in the thermo-NOTE—Radial profiles of global thermodynamic properties derived from spectral modeling. (1) Radius; (2) Temperature; (3) Pseudo-pressure; (4) Pseudo-entropy; (5) Cooling time (6) Reduced  $\chi^2$  of spectral fit.

**Table 1.** Global Cluster Properties from Coarse Binning

$r \pm \Delta r$ (kpc)	$kT$ (keV)	$P$ (keV cm $^{-3}$ )	$K$ (keV cm $^2$ )	$t_c$ ( $10^8$ yr)	$\chi^2_{\text{red}}$
$9.5 \pm 9.5$	$6.18^{+0.80}_{-0.64}$	$2.69^{+0.40}_{-0.34}$	$16.61^{+0.84}_{-0.82}$	$1.83 \pm 0.38$	0.817
$25.4 \pm 6.4$	$5.00^{+0.62}_{-0.54}$	$1.19^{+0.40}_{-0.17}$	$20.11^{+1.36}_{-1.27}$	$2.91 \pm 0.74$	0.699
$39.2 \pm 7.5$	$7.77^{+0.96}_{-0.80}$	$0.99^{+0.16}_{-0.14}$	$47.37^{+3.34}_{-3.06}$	$7.25 \pm 1.87$	0.799
$55.7 \pm 9.0$	$5.59^{+0.57}_{-0.53}$	$0.51^{+0.06}_{-0.06}$	$42.89^{+2.18}_{-2.01}$	$8.25 \pm 1.61$	0.721
$75.5 \pm 10.4$	$8.69^{+1.38}_{-1.05}$	$0.44^{+0.09}_{-0.07}$	$98.16^{+8.08}_{-7.42}$	$19.62 \pm 5.99$	0.761
$101.6 \pm 13.1$	$6.85^{+0.94}_{-0.73}$	$0.24^{+0.04}_{-0.04}$	$97.42^{+7.10}_{-6.80}$	$23.81 \pm 6.52$	0.777
$137.2 \pm 18.7$	$5.57^{+0.75}_{-0.68}$	$0.14^{+0.02}_{-0.02}$	$100.07^{+5.30}_{-4.84}$	$29.50 \pm 6.44$	0.781
$186.0 \pm 27.4$	$13.82^{+3.79}_{-3.16}$	$0.16^{+0.04}_{-0.04}$	$422.34^{+14.30}_{-15.91}$	$116.77 \pm 33.93$	0.872
$247.1 \pm 33.5$	$7.77^{+2.52}_{-1.44}$	$0.06^{+0.02}_{-0.01}$	$309.64^{+18.38}_{-18.74}$	$121.07 \pm 40.73$	0.925
$339.8 \pm 58.1$	$15.20^{+6.98}_{-3.94}$	$0.07^{+0.03}_{-0.02}$	$878.24^{+32.58}_{-33.80}$	$321.72 \pm 128.23$	0.943

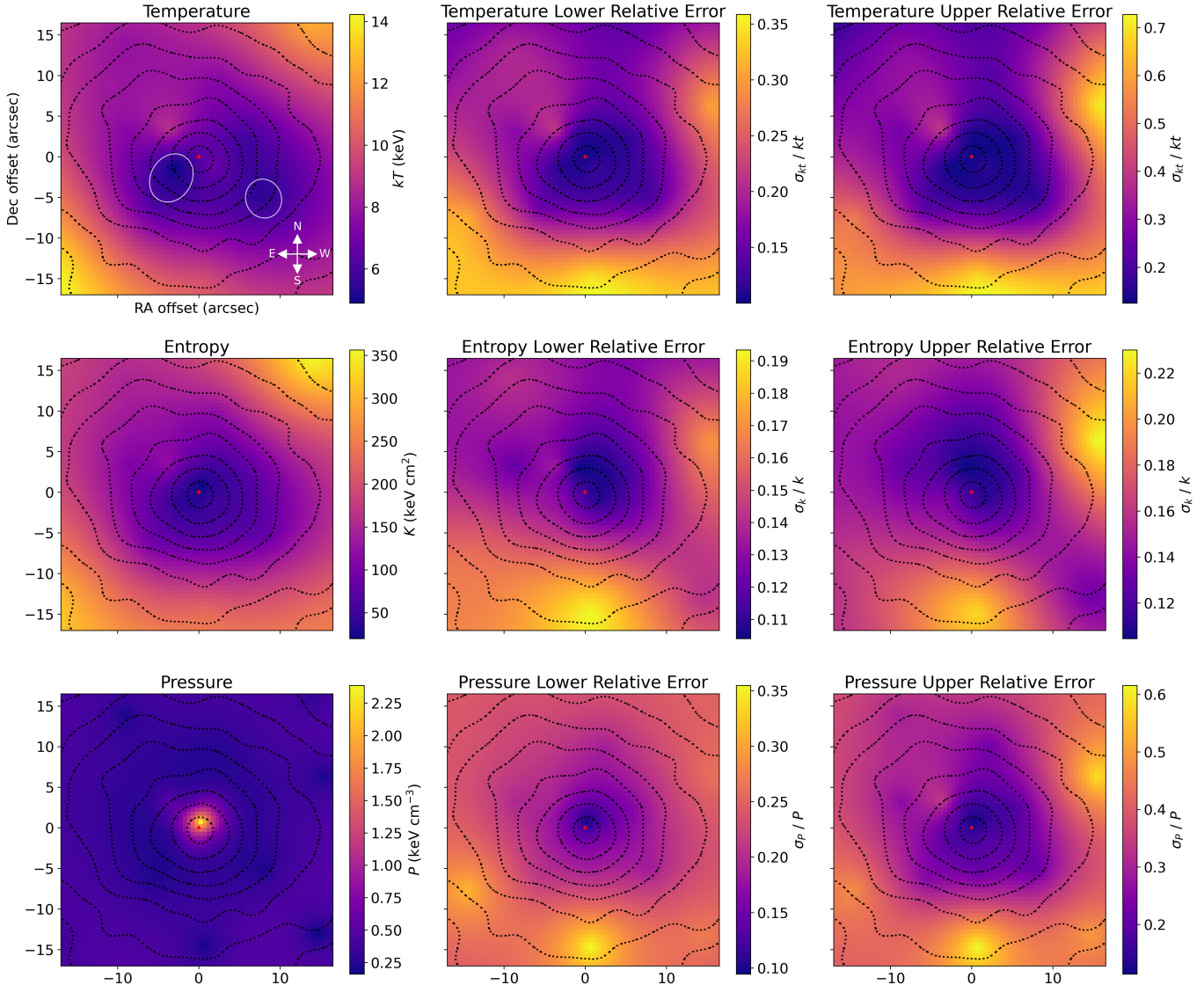


**Figure 3.** Projected thermodynamic maps (temperature, pseudo-entropy, and pseudo-pressure) derived using WVT adaptive binning followed by kriging interpolation, along with the corresponding lower and upper residual error maps. White ellipses in the temperature map indicate the approximate locations of colder clumps. The red cross marks the position of the BCG. Coordinates are shown as offsets from the BCG in arcseconds (1 arcsec = 8.25 kpc).

described in Section 2.1 to derive directional thermodynamic profiles. The results, presented in Figure 5, are consistent with the trends observed in the thermodynamic maps, revealing anisotropies in the central regions. While the SE-NW axis shows a relatively smooth temperature decline to the center, the temperature profile in the SW-NE axis has clear temperature dips and entropy flattening at  $r \approx 180$  kpc. The geometry of the opposed dipolar discontinuities seen in the temperature map of Figure 3 is consistent with cold fronts viewed close to the plane of the sky. This makes it unlikely that the observed flattening of these profiles are due to projection effects. We discuss the possible origin of this feature in Section 4.4. Notably, at the radial bin corre-

sponding to the identified discontinuity at  $r_{\text{sharp}} \approx 160$  kpc, the profiles along the SE-NW axis exhibit similar behavior, characterized by coincident temperature and entropy enhancements as well as a flat pressure profile. These features confirm the presence of two aligned cold fronts along this axis.

### 3. X-RAY IMAGING ANALYSIS

To visually inspect the ICM anisotropies hinted by the thermodynamic maps, we reproject the observations to a common tangent point and create a merged, exposure-corrected image. Again, we use the correspon-

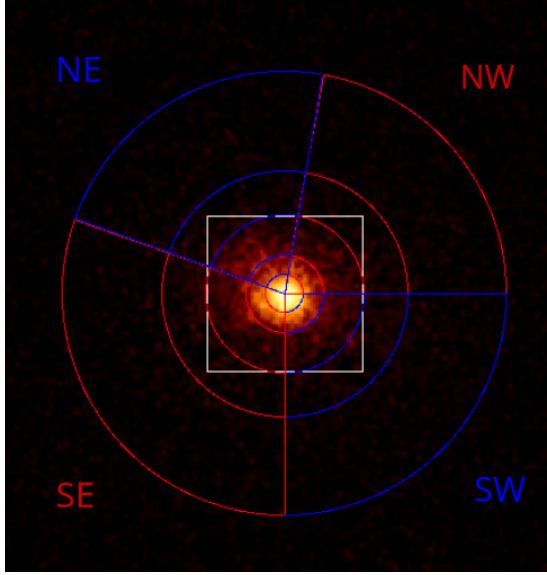


**Figure 4.** Directional sectors and central region used in the analysis. The  $17'' \times 17''$  white box marks the area of the thermodynamic maps. Sectors: NE ( $80^\circ$ – $160^\circ$ ), SE ( $160^\circ$ – $270^\circ$ ), NW ( $0^\circ$ – $80^\circ$ ), SW ( $270^\circ$ – $360^\circ$ ).

**Table 2.** Directional Cluster Properties

Dir.	$r \pm \Delta r$	$kT$	$P$	$K$	$\chi^2_{\text{red}}$
	(kpc)	(keV)	(keV cm $^{-3}$ )	(keV cm $^2$ )	
NE	$17.4 \pm 17.4$	$6.61^{+1.49}_{-1.16}$	$1.50^{+0.38}_{-0.30}$	$31.00^{+2.31}_{-1.93}$	0.944
NE	$52.8 \pm 18.1$	$9.94^{+3.99}_{-2.08}$	$0.78^{+0.32}_{-0.18}$	$94.18^{+5.26}_{-4.82}$	0.746
NE	$107.2 \pm 36.3$	$8.50^{+1.80}_{-1.45}$	$0.30^{+0.07}_{-0.05}$	$139.09^{+7.24}_{-6.17}$	0.814
NE	$183.4 \pm 43.6$	$6.23^{+1.79}_{-1.18}$	$0.09^{+0.03}_{-0.02}$	$190.18^{+16.62}_{-14.80}$	0.724
NE	$313.0 \pm 99.3$	$14.55^{+11.83}_{-6.36}$	$0.07^{+0.06}_{-0.03}$	$895.58^{+70.76}_{-53.51}$	0.919
SE	$17.4 \pm 17.4$	$6.14^{+0.75}_{-0.63}$	$1.74^{+0.25}_{-0.22}$	$22.57^{+2.31}_{-1.93}$	0.699
SE	$52.8 \pm 18.1$	$5.41^{+0.72}_{-0.58}$	$0.56^{+0.11}_{-0.10}$	$39.09^{+2.13}_{-1.97}$	0.747
SE	$107.2 \pm 36.3$	$6.80^{+1.30}_{-0.89}$	$0.23^{+0.05}_{-0.04}$	$103.38^{+5.45}_{-5.34}$	0.788
SE	$183.4 \pm 43.6$	$17.56^{+13.27}_{-5.94}$	$0.23^{+0.04}_{-0.04}$	$508.97^{+25.37}_{-21.77}$	0.767
SE	$313.0 \pm 99.3$	$16.73^{+14.16}_{-5.43}$	$0.09^{+0.04}_{-0.02}$	$875.74^{+44.61}_{-40.46}$	0.861
NW	$17.4 \pm 17.4$	$6.75^{+1.45}_{-1.10}$	$1.67^{+0.38}_{-0.30}$	$30.72^{+2.06}_{-1.80}$	0.867
NW	$52.8 \pm 18.1$	$7.21^{+1.92}_{-1.31}$	$0.65^{+0.11}_{-0.09}$	$64.46^{+4.47}_{-3.92}$	0.700
NW	$107.2 \pm 36.3$	$9.62^{+3.32}_{-2.00}$	$0.29^{+0.10}_{-0.06}$	$176.90^{+10.53}_{-9.40}$	0.755
NW	$183.4 \pm 43.6$	$21.98^{+28.48}_{-9.47}$	$0.27^{+0.33}_{-0.11}$	$745.28^{+39.20}_{-37.50}$	0.693
NW	$313.0 \pm 99.3$	$11.72^{+9.24}_{-4.05}$	$0.06^{+0.04}_{-0.02}$	$727.54^{+64.57}_{-44.37}$	0.913
SW	$17.4 \pm 17.4$	$6.69^{+1.08}_{-0.85}$	$1.88^{+0.33}_{-0.27}$	$24.12^{+1.24}_{-1.15}$	0.772
SW	$52.8 \pm 18.1$	$5.63^{+0.90}_{-0.74}$	$0.54^{+0.13}_{-0.11}$	$41.34^{+2.63}_{-2.32}$	0.801
SW	$107.2 \pm 36.3$	$8.18^{+2.60}_{-1.53}$	$0.25^{+0.08}_{-0.05}$	$130.28^{+8.02}_{-7.42}$	0.686
SW	$183.4 \pm 43.6$	$5.52^{+1.63}_{-1.13}$	$0.08^{+0.03}_{-0.02}$	$146.56^{+16.03}_{-12.99}$	0.851
SW	$313.0 \pm 99.3$	$10.80^{+6.47}_{-2.88}$	$0.06^{+0.04}_{-0.02}$	$546.30^{+38.18}_{-33.34}$	0.987

NOTE—Azimuthal variations in thermodynamic properties. (1) Direction sector; (2) Radius; (3) Temperature; (4) Pseudo-pressure; (5) Pseudo-entropy; (6) Reduced  $\chi^2$  of spectral fit.

dent blanksky files to subtract the scaled backgrounds from the science images.

### 3.1. Residual map

We start by adaptatively smoothing the merged image using the CIAO tool *dmimgadapt* with a gaussian kernel, demanding 16 counts per kernel and a minimum and maximum scale of, respectively, 0.5 and 15 pixels. Then, we proceed to model the radial distribution of the surface brightness with an elliptical 2D double- $\beta$  model, where each component is defined by

$$S(x_i, y_i) = S(r) = A \left[ 1 + \left( \frac{r}{r_c} \right)^2 \right]^{-3\beta+0.5} + C, \quad (7)$$

where

$$r(x_i, y_i) = \frac{\sqrt{x^2(1-e)^2 + y^2}}{1-e}, \quad (8)$$

and

$$\begin{aligned} x &= (x_i - x_0) \cos \theta + (y_i - y_0) \sin \theta, \\ y &= (y_i - y_0) \cos \theta - (x_i - x_0) \sin \theta. \end{aligned} \quad (9)$$

Here,  $(x_0, y_0)$  is the centroid of the cluster,  $e$  is the ellipticity and  $\theta$  is the orientation of the major axis relative to the north in the anti-clockwise direction. The initial values of the cluster shape parameters were calculated using the method of moments of inertia, as described in Plionis et al. (1991), using  $S(r)$  as the generic function. To optimize the parameters we perform a Levenberg-Marquardt optimization to refine the near-optimal solutions and properly estimate the uncertainties. The best fit parameters for the surface brightness model are presented in Table 3. Then, we calculate the normalized residual with  $(\text{Data} - \text{Model})/\text{Data}$ . The residual map in Figure 6 exhibits a relatively low overall amplitude ( $\pm 0.25$ ), but reveals a pronounced dipolar pattern within 15 arcseconds of the BCG. The directional variation in enhanced emission across the cluster radii suggests that this anisotropy is unlikely to be caused by projection effects from a triaxial structure. Instead, it likely arises from a non-symmetric distribution of cold gas, possibly driven by core sloshing. Indeed, the directional surface brightness profiles normalized by the azimuthally averaged brightness shows the oscillatory behavior characteristic of spiral-shaped cold gas structures near the cluster core. These features have been detected in X-ray imaging (Clarke et al. 2004), temperature maps (Fabian et al. 2005) and even in chemical enrichment distributions (Dupke et al. 2007), being also naturally reproduced in simulations (Ascasibar & Markevitch 2006).

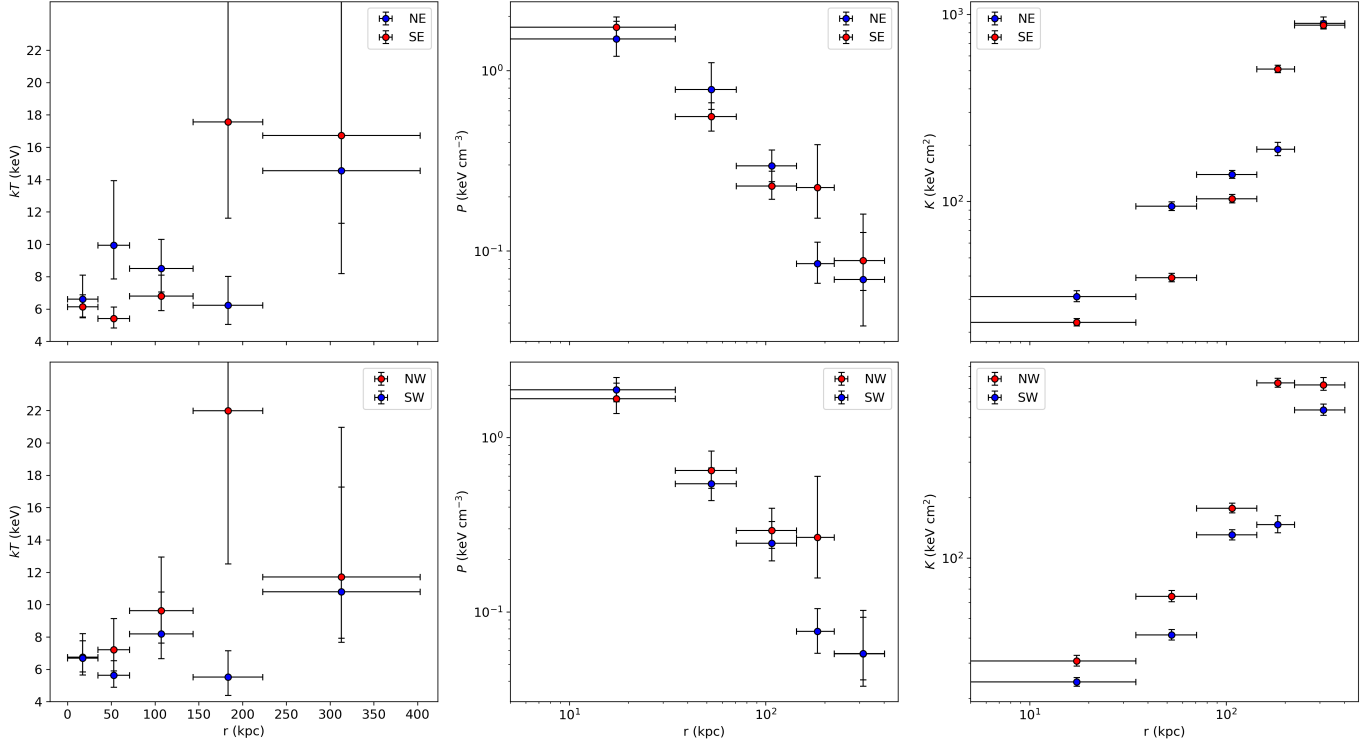


**Figure 5.** Directional projected thermodynamic profiles extracted from sector-shaped annuli. The upper panels compare the NE and SE directions, while the lower panels show the NW versus SW directions.

Another finding from the  $\beta$ -model subtraction is a statistically significant extended depression (residual  $< -0.5$  and local brightness dimming  $\sim 25\%$ ). If we consider that this is a jet-driven X-ray cavity, we can model the bubble as a prolate ellipsoid with semi-axes  $r_1$ ,  $r_2$ , and  $r_3 = r_2$ , where  $r_1$  and  $r_2$  correspond to the semi-major and semi-minor axes of the projected ellipse, respectively. The bubble's physical volume is therefore given by  $V = (4/3)\pi r_1 r_2^2$ . Following standard approaches, we assume this volume contains a population of relativistic electrons in pressure equilibrium with the surrounding ICM. From the cavity's projected elliptical shape, we estimate a volume of  $(2.07 \pm 1.10) \times 10^5$  kpc $^3$ . From the spatially resolved thermodynamic information, we estimate that the necessary energy to inflate such bubble is  $(2.73 \pm 1.86) \times 10^{60}$  erg. Considering that the projected distance between the BCG and the cavity's outermost edge is  $\sim 255$  kpc, we calculate a sound-crossing time of  $188 \pm 22$  Myr. Our calculation of the buoyancy time for this same separation yields  $t_{\text{buoy}} = 236$  Myr, however, it is hard to say if this value is reliable, since estimating the buoyancy requires a well-constrained enclosed mass profile, in order for one to compute the local acceleration. In our case, we try to reproduce Calzadilla et al. (2023) methodology by fitting the deprojected temperature profile with the Vikhlinin et al. (2006) model. Nevertheless, we find that the shape

of the profile is highly sensitive to assumptions about the deprojected temperature structure (e.g., the inclusion of the discontinuity bin, assuming a stable profile beyond  $\sim 430$  kpc). For this reason, we consider the sound-crossing time to be a more robust choice. In any case, from the enclosed-mass profile we obtain by solving the hydrostatic equation, we estimate relevant scale radii to be  $R_{2500} \sim 350$  kpc,  $R_{500} \sim 850$  kpc and  $R_{180} \sim 1480$  kpc. Considering the sound-crossing time as the characteristic timescale for the bubble propagation, our final estimative for the jet power responsible for this possible cavity is  $\log_{10}(P_{\text{cav}}/10^{42} \text{erg s}^{-1}) = 2.66 \pm 0.23$ , consistent with the value reported by Calzadilla et al. (2023) using the  $P_{\text{cav}}-L_{\text{cool}}$  scaling relation (Cavagnolo et al. 2010). Using  $t_{\text{buoy}}$  does not heavily affect the inferred cavity power, as a difference of  $\sim 25\%$  in the timescale results in a change of less than 0.1 dex in the cavity power, well within the original uncertainty. In Section 4.2, we further discuss the feasibility of such a bubble given its observed characteristics, as well as its implications for the cluster's dynamical history.

### 3.2. Morphological Parameters

As previously mentioned, the first indication of the dynamical regularity of SPT2215 arose from the evaluation of its X-ray morphological features. Here, we take

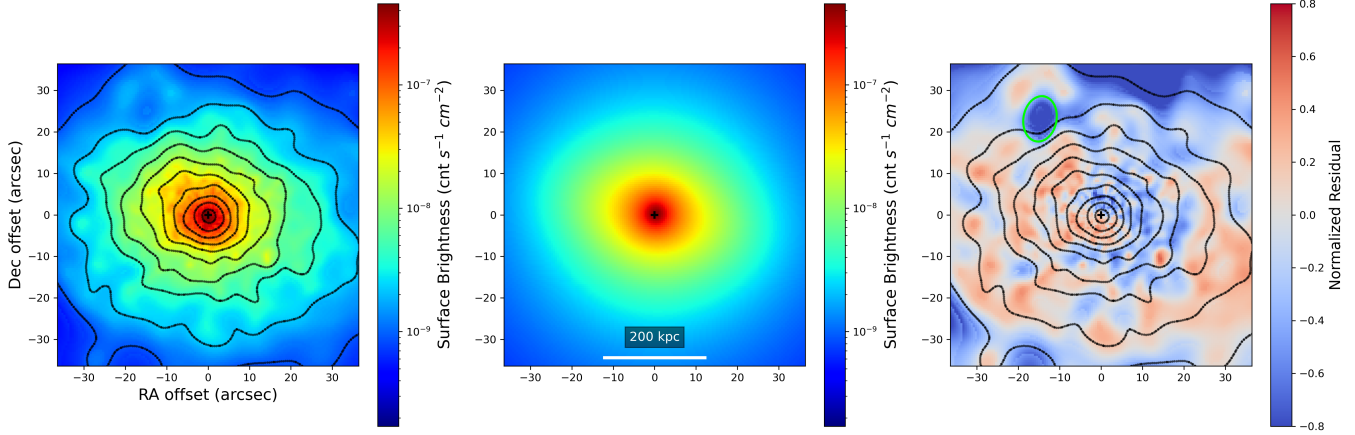


**Figure 6.** Left: Adaptively smoothed X-ray surface brightness map with overlaid contours. Middle: Best-fit double two-dimensional  $\beta$ -model (Equation 7); the optimal parameters are listed in Table 3. Right: Normalized residual map with the surface brightness contours. The green ellipse-centered at  $\alpha = 22^{\text{h}}15^{\text{m}}05.^{\text{s}}1467$ ,  $\delta = -35^{\circ}36'54.^{\text{s}}829$ , with semi-axes of  $5.5 \pm 1$  and  $4.0 \pm 1$  arcseconds and a position angle of  $350^{\circ}$ -encloses the X-ray cavity candidate. The black cross marks the position of the BCG. Coordinates are shown as offsets from the BCG in arcseconds (1 arcsec = 8.25 kpc).

**Table 3.** Double Elliptical  $\beta$ -Model Fit Optimal Parameters

Parameter	Value	Units
(1)	(2)	(3)
$\beta_1$	$0.545 \pm 0.018$	—
$r_{c1}$	$4.9 \pm 1.1$	pixels
$e_1$	$(1.00 \pm 0.70) \times 10^{-2}$	—
$\beta_2$	$0.912 \pm 0.116$	—
$r_{c2}$	$30.3 \pm 4.1$	pixels
$e_2$	$0.314 \pm 0.029$	—
$\theta$	$2.912 \pm 0.016$	radians
$f$	$0.928 \pm 0.030$	—
$A_1$	$(4.58 \pm 0.20) \times 10^{-7}$	$\text{cnt s}^{-1} \text{cm}^{-2}$
$C$	$(1.38 \pm 1.14) \times 10^{-10}$	$\text{cnt s}^{-1} \text{cm}^{-2}$

NOTE—Best-fit parameters for the 2D double- $\beta$  model. The model consists of inner (1) and outer (2) components with ellipticities  $e$ , position angle  $\theta$ , and flux fraction  $f$ , such that  $A_2 = A_1(1 - f)$ .

advantage of our increased image statistics to compute traditional measures: concentration ( $c$ ), centroid shift ( $\omega$ ), and the third-order power ratio ( $P_3/P_0$ ), as well as the morphology index ( $\delta$ ) introduced by Yuan & Han (2020).

The concentration parameter  $c$  quantifies the surface brightness peak strength relative to the overall distribution and is mainly employed to identify the presence of cool cores. Here, we use the definition of  $c$  as the ratio of the integrated X-ray fluxes under the core radius and the outer radius apertures. We choose  $r_{\text{in}} = 100$  kpc and  $r_{\text{out}} = 500$  kpc for consistency with Yuan et al.

(2022), therefore  $c = S_{100 \text{ kpc}}/S_{500 \text{ kpc}}$ .

From Poole et al. (2006), the centroid shift is defined as the standard deviation of the projected separation between the X-ray brightness peak and the model fitted center. These separations are computed along a series of  $n = 20$  decreasing apertures starting from  $r_{\text{out}} = 500$  kpc. Thus,  $\omega = \frac{1}{r_{\text{out}}} \left[ \frac{1}{n-1} \sum_i (\Delta_i - \langle \Delta \rangle)^2 \right]^{1/2}$ , where  $\Delta_i$  is the separation between the brightness peak and the fitted center in the  $i$ th aperture, and  $\langle \Delta \rangle$  is the mean separation value. Here, the center for each aperture is fitted with a single 2D  $\beta$ -model. This metric is sensitive to deviations from symmetry across multiple spatial scales, though for highly peaked surface brightness distributions, it can be dominated by the core contribution, as it is going to be further discussed in Section 4.4.

Finishing the set of traditional morphological parameters, we compute the third-order power ratio  $P_3/P_0$ , which is particularly sensitive to substructures and departures from mirror symmetry (Jeltema et al. 2005). The powers are derived from the multipole expansion of the X-ray surface brightness within  $r_{\text{out}} = 500$  (Buote & Tsai 1995, 1996).

The morphology index  $\delta$  for SPT2215 was previously calculated in Yuan et al. (2022) using one single observation (obsID= 24614), giving  $\delta = 0.10 \pm 0.01$ . Here, we check if this result holds for our merged image. The morphology index is defined as the distance to the line that best separates the dynamical state of a sample of 115 well studied clusters in the  $\kappa - \alpha$  space:  $\delta = 0.68 \log_{10}(\alpha) + 0.73\kappa + 0.21$ . Here, the asymmetric fac-

tor  $\alpha$  and the profile parameter  $\kappa$  are independent measures given by  $\alpha = \sum_{x,y} [s(x,y) - s(x',y')]^2 / \sum_{x,y} s^2(x,y)$ , where  $s(x',y')$  is the flux at the symmetry pixel of  $(x,y)$  with respect to the center, and  $\kappa = (1+e)/\beta$ , where  $e$  and  $\beta$  have the same meaning as before and are extracted from a single elliptical  $\beta$ -model fit. To ensure consistency with the empirical formula for  $\delta$ , we adopt the same aperture and smoothing parameters used in Yuan & Han (2020) when computing  $\alpha$  and  $\kappa$ . We obtain  $\log_{10}(c) = -0.33$ ,  $\log_{10}\omega = -2.57$ ,  $\log_{10}(P_3/P_0) = -6.58$ ,  $\log_{10}(\alpha) = -0.88$ ,  $\kappa = 0.57$ , and  $\delta = 0.028$ . These values are in good agreement to those reported in Yuan et al. (2022), as showed in Figure 7, suggesting that their convergence is not strongly limited by data quality or exposure time. We further discuss in Section 4.4 the numerical correlations among the considered metrics, as well as potential decouplings from the underlying physical phenomenology they are meant to trace.

## 4. DISCUSSION

### 4.1. Core Sloshing

The thermodynamic characterization of SPT2215’s ICM presented in this work reveals notable anisotropies, including what appears to be contact discontinuities along the SE–NW direction, approximately located at the estimated cooling radius,  $r_{cool} = 147 \pm 10$  kpc. The observed sharp increase in temperature and entropy within the corresponding radial bin, accompanied by an approximately constant pressure, are well-established signatures of cold fronts. In Figure 5, the SE–NW temperature and entropy profiles are consistent with a core oscillation within the boundaries of  $r_{cool}$ , where, below  $r_{cool}$ , the gas in the SE is considerably colder compared to other directions. This mismatch then inverts just beyond  $r_{cool}$ , with the entropy finally converging in the 210–410 kpc bin. This radial behaviour aligns with the central emission excess distribution seen in the residual map of Figure 6, which shows clear spiral patterns along multiple scales.

Spatial resolution limits the detection of cold fronts in clusters as distant as SPT2215. Even with the combined observations analyzed in this work, we do not detect them solely from the surface brightness. Nevertheless, the scenario supported by our spectral modeling is not unexpected, as many cool-core clusters contain signatures of cold fronts. The hydrodynamic simulations of mergers done by Ascasibar & Markevitch (2006) revealed that core sloshing can induce such discontinuities given a sufficiently steep entropy profile. When fitting

the azimuthally-averaged entropy profile with a power law, we get a slope of  $1.12 \pm 0.12$ , as predicted by self-similar evolution models (Tozzi & Norman 2001; Voit et al. 2005; Cavagnolo et al. 2009). Restricting the fit for the  $[0.01\text{--}0.08]r_{180}$  range, we find a slope of  $1.25 \pm 0.18$ . The mean scaled entropy profile slope of cold front clusters reported by Ghizzardi et al. (2010) is  $\alpha[(0.01\text{--}0.08)r_{180}] = 1.22 \pm 0.01$ . Although our central value is consistent with theirs, the uncertainty is large enough that we cannot distinguish this slope from the self-similar expectation at a statistically significant level. If the entropy profile is indeed steeper in this radial range, a past off-axis interaction with a gas-poor substructure could have significantly perturbed the low-entropy gas in the cluster’s core, giving rise to sloshing cold fronts that propagated outward with time, stalling approximately at the cooling radius.

It is worth noting the coincident SE–NW orientation of the extended blue filaments in the BCG, as observed by archival HST/WFC3-UVIS F200LP imaging (Program ID: idgbt2020). Magnetohydrodynamic simulations indicate that sloshing-driven motions can amplify magnetic field strengths along shear flows, suppress gas mixing, and promote anisotropic thermal conduction (ZuHone et al. 2011, 2013), which could be a plausible mechanism for the apparent SE–NW orientation of the filaments. A minimum local cooling time over the free-fall time  $t_{cool}/t_{ff}$  below  $\sim 10$  indicate conditions favorable for thermal instability and efficient multiphase condensation in the circumgalactic medium (Voit et al. 2015). We find a  $\min(t_{cool}/t_{ff}) \approx 8$  at  $r \approx 25$  kpc, indicating that the resulting condensation is fueling the intense starburst in the BCG (Calzadilla et al. 2023).

### 4.2. Ghost Bubble Candidate

Let us now discuss the plausibility of the possible X-ray cavity revealed by our imaging analysis. The majority of cool core clusters harbour radio sources and bubble-like structures, filled with relativistic electrons, produced by AGN jets, likely triggered by accretion of cold gas onto the central supermassive black hole. The propagation of these bubbles is an efficient way of injecting energy into the central regions of the cluster, since it creates pressure waves that are viscously dissipated throughout the ICM. The ASKAP weak radio detection at 0.9 GHz surrounding SPT2215’s BCG indicates ongoing AGN feedback. We do not expect GHz emission from a bubble with such high age ( $t \approx 190$  Myr), making it a ghost bubble candidate. Considering the observed cavity properties, we calculate a jet

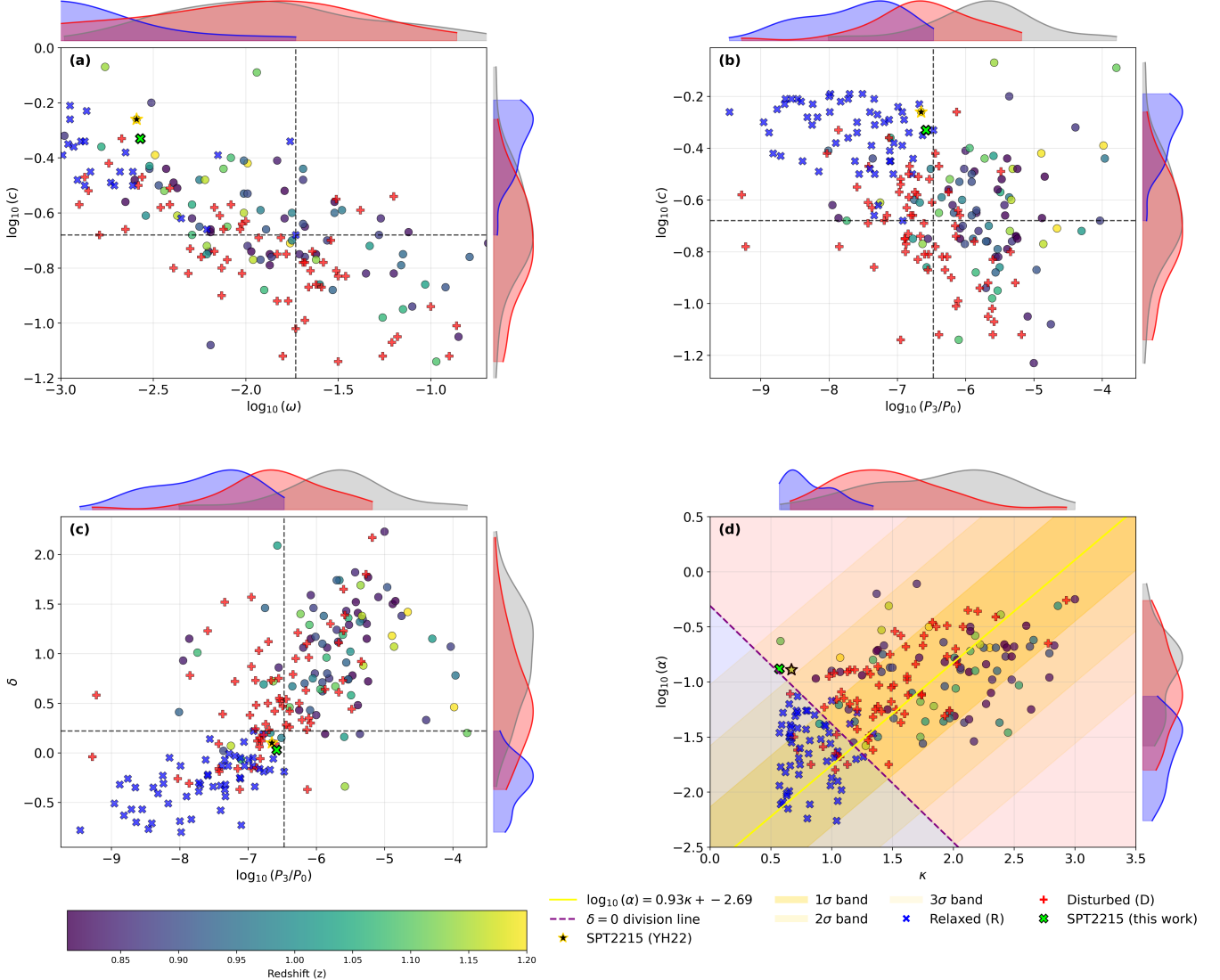


**Figure 7.** Parameter spaces of the morphological parameters considered in this work. Blue X's and red crosses represent the relaxed and disturbed clusters from the test sample of Yuan & Han (2020), respectively, which have independent dynamical classifications. Circles indicate the selected high-redshift subsample ( $0.8 < z < 1.2$ ) from Yuan et al. (2022). The blue, red, and grey shaded regions on the outside of the plotting frames illustrate the distribution of relaxed, disturbed, and high-redshift clusters, respectively, in the parameter spaces. Dashed black lines mark the threshold values limiting the region occupied by relaxed clusters.

power that is consistent with the value obtained from the  $P_{\text{cav}}-L_{\text{cool}}$  relation (Cavagnolo et al. 2010) reported by Calzadilla et al. (2023), but with a significant uncertainty improvement:  $\log_{10}(P_{\text{cav}}/10^{42}\text{erg s}^{-1}) = 2.66 \pm 0.23$  against  $\log_{10}(P_{\text{cav}}/10^{42}\text{erg s}^{-1}) = 2.6 \pm 0.3$  (stat)  $\pm 0.8$  (int. scatter). Naturally, there are hard limits on the cavity's measurable features conditioned to spatial resolution and growth limit. In our case, the cavity's dimensions exceed the detection threshold for the considered redshift, while the high mean temperature of the surrounding ICM places it below the expected growth limit. From a sample of 148 cavities present in 69 targets, Shin et al. (2016) found a linear correlation between

the cavity area and its projected distance expressed by  $\log_{10}(A) = (1.94 \pm 0.04) \log_{10}(D) + 0.02 \pm 0.05$ . Given  $A \approx 4700 \pm 1400 \text{ kpc}^2$  and  $D \approx 230 \text{ kpc}$ , we find a deviation of  $\Delta \log_{10}(A) \approx -0.93$  from the considered correlation, which corresponds to nearly  $3\sigma$ . For this projected distance, the cavity's size should be about an order of magnitude larger. This could be seen as a main caveat of this observed feature as a real structure. On the other hand, it is worth to consider that the sample of clusters used by Shin et al. (2016) did not include any ghost bubbles. The growth conditions in high-redshift clusters can differ significantly due to evolving ICM properties (e.g., magnetic pressure, viscosity, thermal conduction),

which may affect the morphology of highly evolved bubbles and cause deviations from general scaling relations (see Bourne & Yang 2023 for a review).

### 4.3. Cooling-Feedback Cycle

Strong evidence supports the so called cooling-feedback model, in which radiative cooling and feedback from the central supermassive black hole mutually influence and constrain each other in a self-regulating manner (eg., Dunn & Fabian 2006; Main et al. 2017; Calzadilla et al. 2024). Following the feedback-regulated precipitation framework developed by Voit et al. (2017) for cluster cores, we can attempt to qualitatively assess the current phase of SPT2215. In order to do so, we consider three independent probes: The time since the AGN restarted, the minimum value of  $t_{\text{cool}}/t_{\text{ff}}$  and the star formation rate in the BCG. If we take the cavity age calculated in Section 3.1 ( $t_{\text{cav}} \approx 190 \pm 20$  Myr) as a lower limit for the time since the last outburst, then SPT2215 would be likely in the early phase of progression towards a long-lasting self-regulated cycle. The found  $\min(t_{\text{cool}}/t_{\text{ff}}) \approx 8$  is under the threshold for thermal instability, indicating that the isentropic region out to  $r \approx 25$  kpc is still not completely formed. Considering that a steep central entropy gradient can only develop following the formation of a stable hot halo, a process expected to occur no earlier than  $z \sim 2\text{--}2.5$  for massive systems (see Overzier 2016), a cluster observed at  $z = 1.16$  would be expected to have at most roughly 2 Gyr to have established a stable cooling-feedback loop. Therefore, it is reasonable to conclude that SPT2215 is, at most, about to enter the second long-lasting self-regulated cycle. The idealized simulation of a cluster core done by Li et al. (2015) (see Figure 2 of their paper) showed that the onset of star formation in the BCG can occur rapidly after the outburst event, leading to a drastic increase in the local buildup of cold gas. On the other hand, the response of  $\min(t_{\text{cool}}/t_{\text{ff}})$  to the outflows happens in a considerably longer timescale. This delay arises from the fact that, before a stable isentropic core can develop, the bulk low-entropy gas needs to be removed or reprocessed via turbulence, mixing and condensation.  $\sim 190$  Myr after the second outburst, the star formation rate would have enough time to be already stabilized around its peak, explaining the massive starburst in the BCG ( $\text{SFR} = 320^{+230}_{-140} M_{\odot} \text{yr}^{-1}$ ) (Calzadilla et al. 2023). The thermodynamic profiles along the supposed bipolar outflow axis (SW–NE) show notable deviations compared to the SE–NW direction, including a central temperature bump in the NE direction (Figure 5) and entropy flattening at intermediate scales (Figure 2). These asymmetries likely reflect enhanced inho-

mogeneities and turbulence induced by the recent AGN activity. In particular, uplift and mixing along the outflow axis can lead to transient entropy irregularities and deviations from hydrostatic equilibrium. As the system evolves toward a fully precipitation-regulated state, buoyancy and turbulent damping are expected to progressively erase these features, leading to a more symmetric and smoother thermodynamic structure.

### 4.4. Limitations of the Morphology-based Classification

The use of morphological parameters as proxies for cluster relaxation is based on the principle that the 2D projection of the emission reliably traces dynamical phenomena. Given X-ray observables and the underlying intrinsic state, the morphological measures serve as estimators of the true dynamical state. The mapping is non-injective, that is, distinct intrinsic states may produce similar 2D features as a result of projection or fundamentally different physical conditions, which is why classifications based on single measures must be taken with caution. Instead, the set of morphological parameters usually populate a multidimensional space where certain regions are empirically associated to relaxed and perturbed clusters. Thresholds are typically determined using a sample of clusters with independently confirmed dynamical states, or derived numerically from mock images of simulated clusters.

Let us now explore potential caveats of the presented framework and how it relates to the current classification of SPT2215. First, thresholds are naturally set to maximize the purity of relaxed/perturbed subsamples, which inevitably tends to misclassify systems with intermediate dynamical stages. This effect is likely to be more prevalent for high-redshift clusters due to the expected higher merger rate. Second, a fixed threshold assumes either that (1) the correlation between the 2D observable and a given 3D property associated to the dynamical state does not have a significant mass- or redshift-dependent evolution, or (2) the functional form of this evolution is known *a priori*, such that the parameter can be appropriately rescaled. This matter was addressed by Cao et al. (2021) (hereafter CBV21) using Mock-X (Barnes et al. 2021) to generate synthetic X-ray images of clusters from the IllustrisTNG, BAHAMAS and MACSIS cosmological hydrodynamical simulations. They evaluated various aspects of the established morphological measures, including how they are correlated to each other and to 3D theoretical parameters extracted from the simulated halos. Regarding redshift evolution, although many specific considerations can be made about the impact of subgrid physics and numerical

resolution on the observed trends for each simulation, CBV21 found that generally all morphological parameters exhibit some level of redshift evolution. This result highlights the critical importance of correctly modeling the functional form of this dependence.

Figure 7 shows the distribution of clusters in the relevant parameter spaces for three subsamples: relaxed ( $R$ ), disturbed ( $D$ ) and high-redshift ( $0.8 < z < 1.2$ ) clusters. We may give special attention to parameters that are somehow dependent on the cluster's central emission cuspiness: more readily, the concentration index ( $c$ ), and indirectly, the centroid shift ( $\omega$ ). First, we notice from Figure 7 that, with the exception of  $c$  and  $\omega$ , all other parameters tend to produce a displaced distribution towards the unrelaxed end for the high-redshift subsample. Additionally,  $c \times \omega$  gives the highest contamination for a relaxed region among all parameter spaces. We shall briefly discuss the origin of this trend. To begin, we must acknowledge a degree of numerical degeneracy between  $c$  and  $\omega$ , since a centrally peaked brightness distribution can suppress the measured centroid displacements across all apertures, weighting the centroid more strongly toward the core. Naturally, if one has to use a single morphological parameter to classify the dynamical state of a test sample, this feature can be seen as a strength, since it somehow captures two different aspects of the emission distribution: the central cuspiness, indicating the presence of a structured cool core, and asymmetries, quantifying the presence of substructures. For large samples, it can be effective in distinguishing highly dynamically disturbed clusters from very relaxed ones. For instance, Maughan et al. (2008) used a core-excised  $\omega$  as a single relaxation proxy for a sample of 115 clusters in the range  $0.1 < z < 1.3$ , finding a clear absence of highly relaxed clusters at  $z > 0.5$ . We argue that this degeneracy becomes particularly problematic for high-redshift clusters when the core contribution is included. We suggest that the low purity for  $c \times \omega$  seen in Figure 7(a) is caused by a combination of this degeneracy and a poorly modeled redshift dependence of  $c$ .

The surface brightness peakiness ( $p$ ) from SPA is a more refined version of  $c$ , since it is measured under a same scaled surface brightness level by assuming a self-similar model, and it includes a  $(1+z)$  term, which results in a nearly constant fraction of peaked clusters across redshift. The other two statistics are the symmetry ( $s$ ) and the alignment ( $a$ ) as defined in Mantz et al. (2015). For SPT2215, the SPA measurements are  $s = 1.24 \pm 0.15$ ,  $p = -0.46 \pm 0.04$  and  $a = 1.42 \pm 0.16$

(Calzadilla et al. 2023). Upon visual inspection of Figure 2 of their paper, one can notice that the  $a \times s$  space yields a higher contamination compared to  $s \times p$  and  $a \times p$ , suggesting that  $p$  carries a greater weight in distinguishing the dynamical state. CBV21 points out that the redshift evolution of  $p$ , even with the  $(1+z)$  term, is too strong, producing larger subsamples of relaxed clusters with increasing redshift. By fitting the morphological parameters with a  $(1+z)^{-\beta}$  factor, they found  $\beta(s) = 0.59 \pm 0.18$ ,  $\beta(p) = 3.42 \pm 0.49$  and  $\beta(a) = 1.38 \pm 0.21$ . Applying these corrections to the original SPA measurements, we get  $s_z = 1.04 \pm 0.16$ ,  $p_z = -1.60 \pm 0.17$  and  $a_z = 0.96 \pm 0.17$ . For the sake of comparison, if we keep the original relaxation thresholds ( $s > 0.87$ ,  $p > -0.82$  and  $a > 1.00$ ), then  $s$  marginally passes the criterion,  $p$  strongly fails and  $a$  remains in the borderline. Therefore, once the redshift evolution is accounted for, we find a scenario that is much more consistent with an intermediate dynamical state, which matches the near-zero morphology index  $\delta = 0.028$  and the more central  $\log_{10}(P_3/P_0) = -6.58$  value (although more consistent with the disturbed subsample distribution in this case).

#### 4.5. Physical Interpretation of Cuspiness Enhancement

It seems that, at high-redshift, a centrally peaked emission is not as strong an indicator of a virialized state as it is in the local universe. The most straightforward reason would be that a surviving post-merger cool core under a high merger rate regime, can retain a high peakiness, even when the cluster remains dynamically disturbed. But we argue this can also be the contribution of competing physical processes, particularly related to a not yet fully regulated AGN feedback cycle at earlier cosmic times, as pointed by Calzadilla et al. (2024). Our combined analysis, together with the interpretation given in Section 4.4, supports the idea that SPT2215 is experiencing extreme thermal imbalance during the period between an outburst event and the development of a two-phase entropy structure, which can be creating a cooling-dominated regime that amplifies the surface brightness cuspiness while not necessarily reflecting strong virialization. Thus, what we might be seeing in SPT2215 is a short transient state in which feedback has been recently triggered and has not yet had sufficient time to offset the overwhelming cooling, which in turn dominates the central X-ray emission and bias morphological criteria towards relaxation.

## 5. SUMMARY

We present a detailed revision of the dynamical state of the high-redshift galaxy cluster SPT-CL J2215-3537,

based on a comprehensive X-ray analysis of all currently available Chandra observations, and provide a discussion on the use of morphological statistics to assess relaxation in the high-redshift regime. Our results and conclusions can be summarized as follows:

1. The thermodynamic characterization of SPT2215 reveals significant anisotropies, including off-center clumps of colder gas toward the eastern direction and features consistent with cold front signatures near the cooling radius along the SE–NW axis. The  $\beta$ -model-subtracted residual show a central dipolar pattern along the SE–NW direction and arc-shaped surface brightness excess across different scales, both features consistent with a core sloshing scenario.
2. We propose that a past off-axis merger with a gas-poor structure triggered core sloshing. The steep entropy profile in the core would allow the resulting oscillatory, subsonic gas motions to generate the observed cold fronts near the edges of the cool core. These bulk motions may also create a preferential channel for the inflow of low-entropy gas, potentially enhancing star formation along the SE–NW axis. Even if the cluster does not qualify as the most distant relaxed cluster, as claimed by previous works, to our knowledge it is the most distant cluster where sloshing cold fronts were observed.
3. The residual map reveals a candidate ghost bubble located approximately 230 kpc to the NW. Although the observed features of the cavity deviate significantly from known empirical relations, the derived  $P_{\text{cav}}$  is consistent with the previous estimate from the  $P_{\text{cav}}\text{-}L_{\text{cool}}$  scaling relation, indicating that radiative cooling is currently outweighing AGN feedback.
4. The main properties of SPT2215’s core can be qualitatively explained by the precipitation-regulated framework developed by [Voit et al. \(2015\)](#). Our combined analysis indicates that SPT2215 is currently in the early phase of progression towards a long-lasting self-regulated cooling-feedback cycle. At present, condensation appears to be mostly confined to the inner regions ( $\sim 25 \pm 6$  kpc) and the entropy distribution at each radius is still inhomogeneous out to  $\sim 180 \pm 40$  kpc along the SW–NE axis.
5. We compute traditional morphological parameters for our merged X-ray image and find a morphology

index  $\delta = 0.028$  and power ratio  $\log_{10}(P_3/P_0) = -6.58$  consistent with a mildly disturbed system, but a concentration  $\log_{10}(c) = -0.33$  and centroid shift  $\log_{10}(\omega) = -2.57$  characteristic of highly relaxed systems. We discuss evidence suggesting that these values are biased due to a strong redshift-evolution of morphological parameters associated to the central emission cuspiness. We reevaluate the SPA criteria, which had previously classified SPT2215 as dynamically relaxed, noticing that the peakiness statistic carries a greater weight in placing the system in the relaxed locus of the parameter space. When applying the redshift dependences indicated by [CBV21](#), we find new SPA measurements ( $s_z = 1.04 \pm 0.16$ ,  $p_z = -1.60 \pm 0.17$  and  $a_z = 0.96 \pm 0.17$ ), which are now consistent with an intermediate dynamical state.

6. We propose that the strong redshift-dependence of the peakiness and concentration parameters is related to an undeveloped cooling-feedback cycle at high-redshift. In this sense, a peaked cluster at high-redshift would not imply a virialized dynamical state as strongly as it does at low redshift due to the increased prevalence of transient or rapidly evolving core conditions at earlier cosmic times. Spatially resolved X-ray analysis of other similar and, especially, higher redshift clusters will be crucial to further test this hypothesis (Bessa et al., in prep).

Our joint analysis indicates that SPT2215 is a mildly disturbed high-redshift cluster hosting a cool core. We reiterate the relevance of follow-up observations of SPT2215, since this system represents an ideal case for understanding the cooling-feedback cycle and out-of-equilibrium conditions in the cores of high-redshift galaxy clusters. Observations with the future Advanced X-ray Imaging Satellite (AXIS) ([Russell et al. 2024](#)) will be particularly decisive, allowing for enough statistics to generate thermodynamic maps with significantly enhanced spatial resolution and coverage, probing potential new features such as gas motions beyond the cold fronts, abundance distributions, fainter X-ray cavities and more. Meanwhile, additional independent constraints on clusters dynamical state will be particularly important, such as those, that can be provided through measurements of  $f_{\text{ICL}}$  in a set of bands that best probe the intracluster light excess, corresponding to the rest-frame wavelength interval 5200–7300 Å ([Jiménez-Teja et al. 2024](#)).

<sup>1</sup> We are deeply grateful to Dr. Alberto Ardila and  
<sup>2</sup> Vinicius Sanches for the insightful discussions. This  
<sup>3</sup> work was supported by the *Coordenação de Aper-  
<sup>4</sup> feiçoamento de Pessoal de Nível Superior* (CAPES)  
<sup>5</sup> and the *Fundação de Amparo à Pesquisa do Es-  
<sup>6</sup> tado do Rio de Janeiro* (FAPERJ). R.A.D. acknowl-  
<sup>7</sup> edges partial support from CNPq grant 312565/2022-4.  
<sup>8</sup> Y.J-T. acknowledges financial support from the State  
<sup>9</sup> Agency for Research of the Spanish MCIU through  
<sup>10</sup> Center of Excellence Severo Ochoa award to the In-  
<sup>11</sup> stituto de Astrofísica de Andalucía CEX2021-001131-  
<sup>12</sup> S funded by MCIN/AEI/10.13039/501100011033, and  
<sup>13</sup> from the grant PID2022-136598NB-C32 Estallidos and  
<sup>14</sup> project ref. AST22-00001-Subp-15 funded by the EU-  
<sup>15</sup> NextGenerationEU. This research employs a list of  
<sup>16</sup> Chandra datasets, obtained by the Chandra X-ray Ob-  
<sup>17</sup> servatory, contained in DOI: [10.25574/cdc.504](https://doi.org/10.25574/cdc.504), and  
<sup>18</sup> the software provided by the High Energy Astrophysics  
<sup>19</sup> Science Archive Research Center (HEASARC), which  
<sup>20</sup> is a service of the Astrophysics Science Division at  
<sup>21</sup> NASA/GSFC. We also used Ned Wright's CosmoCalc  
<sup>22</sup> (Wright 2006).

## REFERENCES

Allen, S. W., Rapetti, D. A., Schmidt, R. W., et al. 2008, MNRAS, 383, 879, doi: [10.1111/j.1365-2966.2007.12610.x](https://doi.org/10.1111/j.1365-2966.2007.12610.x)

Allen, S. W., Schmidt, R. W., Ebeling, H., Fabian, A. C., & van Speybroeck, L. 2004, MNRAS, 353, 457, doi: [10.1111/j.1365-2966.2004.08080.x](https://doi.org/10.1111/j.1365-2966.2004.08080.x)

Allen, S. W., Schmidt, R. W., & Fabian, A. C. 2002, MNRAS, 334, L11, doi: [10.1046/j.1365-8711.2002.05601.x](https://doi.org/10.1046/j.1365-8711.2002.05601.x)

Anders, E., & Grevesse, N. 1989, GeoCoA, 53, 197, doi: [10.1016/0016-7037\(89\)90286-X](https://doi.org/10.1016/0016-7037(89)90286-X)

Angelinelli, M., Ettori, S., Dolag, K., Vazza, F., & Ragagnin, A. 2023, A&A, 675, A188, doi: [10.1051/0004-6361/202245782](https://doi.org/10.1051/0004-6361/202245782)

Applegate, D. E., Mantz, A., Allen, S. W., et al. 2016, MNRAS, 457, 1522, doi: [10.1093/mnras/stw005](https://doi.org/10.1093/mnras/stw005)

Arnaud, K. A. 1996, in Astronomical Society of the Pacific Conference Series, Vol. 101, Astronomical Data Analysis Software and Systems V, ed. G. H. Jacoby & J. Barnes, 17

Ascasibar, Y., & Markevitch, M. 2006, ApJ, 650, 102, doi: [10.1086/506508](https://doi.org/10.1086/506508)

Bahcall, N. A., & Cen, R. 1993, ApJL, 407, L49, doi: [10.1086/186803](https://doi.org/10.1086/186803)

Barnes, D. J., Vogelsberger, M., Pearce, F. A., et al. 2021, MNRAS, 506, 2533, doi: [10.1093/mnras/stab1276](https://doi.org/10.1093/mnras/stab1276)

Bleem, L. E., Bocquet, S., Stalder, B., et al. 2020, ApJS, 247, 25, doi: [10.3847/1538-4365/ab6993](https://doi.org/10.3847/1538-4365/ab6993)

Bourne, M. A., & Yang, H.-Y. K. 2023, Galaxies, 11, 73, doi: [10.3390/galaxies11030073](https://doi.org/10.3390/galaxies11030073)

Buote, D. A., & Tsai, J. C. 1995, ApJ, 452, 522, doi: [10.1086/176326](https://doi.org/10.1086/176326)

—. 1996, ApJ, 458, 27, doi: [10.1086/176790](https://doi.org/10.1086/176790)

Calzadilla, M. S., Bleem, L. E., McDonald, M., et al. 2023, ApJ, 947, 44, doi: [10.3847/1538-4357/acc6c2](https://doi.org/10.3847/1538-4357/acc6c2)

Calzadilla, M. S., McDonald, M., Benson, B. A., et al. 2024, ApJ, 976, 169, doi: [10.3847/1538-4357/ad8916](https://doi.org/10.3847/1538-4357/ad8916)

Cao, K., Barnes, D. J., & Vogelsberger, M. 2021, MNRAS, 503, 3394, doi: [10.1093/mnras/stab605](https://doi.org/10.1093/mnras/stab605)

Cappellari, M., & Copin, Y. 2003, MNRAS, 342, 345, doi: [10.1046/j.1365-8711.2003.06541.x](https://doi.org/10.1046/j.1365-8711.2003.06541.x)

Cavagnolo, K. W., Donahue, M., Voit, G. M., & Sun, M. 2009, ApJS, 182, 12, doi: [10.1088/0067-0049/182/1/12](https://doi.org/10.1088/0067-0049/182/1/12)

Cavagnolo, K. W., McNamara, B. R., Nulsen, P. E. J., et al. 2010, ApJ, 720, 1066, doi: [10.1088/0004-637X/720/2/1066](https://doi.org/10.1088/0004-637X/720/2/1066)

Clarke, T. E., Blanton, E. L., & Sarazin, C. L. 2004, ApJ, 616, 178, doi: [10.1086/424911](https://doi.org/10.1086/424911)

Diaferio, A. 1999, MNRAS, 309, 610, doi: [10.1046/j.1365-8711.1999.02864.x](https://doi.org/10.1046/j.1365-8711.1999.02864.x)

—. 2009, arXiv e-prints, arXiv:0901.0868, doi: [10.48550/arXiv.0901.0868](https://doi.org/10.48550/arXiv.0901.0868)

Diaferio, A., & Geller, M. J. 1997, *ApJ*, 481, 633, doi: [10.1086/304075](https://doi.org/10.1086/304075)

Diehl, S., & Statler, T. S. 2006, *MNRAS*, 368, 497, doi: [10.1111/j.1365-2966.2006.10125.x](https://doi.org/10.1111/j.1365-2966.2006.10125.x)

Dunn, R. J. H., & Fabian, A. C. 2006, *MNRAS*, 373, 959, doi: [10.1111/j.1365-2966.2006.11080.x](https://doi.org/10.1111/j.1365-2966.2006.11080.x)

Dupke, R., White, III, R. E., & Bregman, J. N. 2007, *ApJ*, 671, 181, doi: [10.1086/522194](https://doi.org/10.1086/522194)

Ettori, S., Morandi, A., Tozzi, P., et al. 2009, *A&A*, 501, 61, doi: [10.1051/0004-6361/200810878](https://doi.org/10.1051/0004-6361/200810878)

Evrad, A. E., Metzler, C. A., & Navarro, J. F. 1996, *ApJ*, 469, 494, doi: [10.1086/177798](https://doi.org/10.1086/177798)

Fabian, A. C., Sanders, J. S., Taylor, G. B., & Allen, S. W. 2005, *MNRAS*, 360, L20, doi: [10.1111/j.1745-3933.2005.00037.x](https://doi.org/10.1111/j.1745-3933.2005.00037.x)

Fruscione, A., McDowell, J. C., Allen, G. E., et al. 2006, in Society of Photo-Optical Instrumentation Engineers (SPIE) Conference Series, Vol. 6270, Observatory Operations: Strategies, Processes, and Systems, ed. D. R. Silva & R. E. Doxsey, 62701V, doi: [10.1117/12.671760](https://doi.org/10.1117/12.671760)

Ghizzardi, S., Molendi, S., Pizzolato, F., & De Grandi, S. 2004, *ApJ*, 609, 638, doi: [10.1086/421314](https://doi.org/10.1086/421314)

Ghizzardi, S., Rossetti, M., & Molendi, S. 2010, *A&A*, 516, A32, doi: [10.1051/0004-6361/200912496](https://doi.org/10.1051/0004-6361/200912496)

Haiman, Z., Mohr, J. J., & Holder, G. P. 2001, *ApJ*, 553, 545, doi: [10.1086/320939](https://doi.org/10.1086/320939)

Hashimoto, Y., Böhringer, H., Henry, J. P., Hasinger, G., & Szokoly, G. 2007, *A&A*, 467, 485, doi: [10.1051/0004-6361:20065125](https://doi.org/10.1051/0004-6361:20065125)

HI4PI Collaboration, Ben Bekhti, N., Flöer, L., et al. 2016, *A&A*, 594, A116, doi: [10.1051/0004-6361/201629178](https://doi.org/10.1051/0004-6361/201629178)

Jeltema, T. E., Canizares, C. R., Bautz, M. W., & Buote, D. A. 2005, *ApJ*, 624, 606, doi: [10.1086/428940](https://doi.org/10.1086/428940)

Jiménez-Teja, Y., Dupke, R. A., Lopes, P. A. A., & Dimauro, P. 2024, *ApJL*, 960, L7, doi: [10.3847/2041-8213/ad181a](https://doi.org/10.3847/2041-8213/ad181a)

Jiménez-Teja, Y., Dupke, R. A., Lopes, P. A. A., & Vilchez, J. M. 2023, *A&A*, 676, A39, doi: [10.1051/0004-6361/202346580](https://doi.org/10.1051/0004-6361/202346580)

Lau, E. T., Kravtsov, A. V., & Nagai, D. 2009, *ApJ*, 705, 1129, doi: [10.1088/0004-637X/705/2/1129](https://doi.org/10.1088/0004-637X/705/2/1129)

Lee, W., Cha, S., Jee, M. J., et al. 2023, *ApJ*, 945, 71, doi: [10.3847/1538-4357/acb76b](https://doi.org/10.3847/1538-4357/acb76b)

Li, Y., Bryan, G. L., Ruszkowski, M., et al. 2015, *ApJ*, 811, 73, doi: [10.1088/0004-637X/811/2/73](https://doi.org/10.1088/0004-637X/811/2/73)

Mahdavi, A., Hoekstra, H., Babul, A., & Henry, J. P. 2008, *MNRAS*, 384, 1567, doi: [10.1111/j.1365-2966.2007.12796.x](https://doi.org/10.1111/j.1365-2966.2007.12796.x)

Main, R. A., McNamara, B. R., Nulsen, P. E. J., Russell, H. R., & Vantyghem, A. N. 2017, *MNRAS*, 464, 4360, doi: [10.1093/mnras/stw2644](https://doi.org/10.1093/mnras/stw2644)

Mantz, A. B., Allen, S. W., Morris, R. G., et al. 2014, *MNRAS*, 440, 2077, doi: [10.1093/mnras/stu368](https://doi.org/10.1093/mnras/stu368)

—. 2015, *MNRAS*, 449, 199, doi: [10.1093/mnras/stv219](https://doi.org/10.1093/mnras/stv219)

Mantz, A. B., Morris, R. G., Allen, S. W., et al. 2022, *MNRAS*, 510, 131, doi: [10.1093/mnras/stab3390](https://doi.org/10.1093/mnras/stab3390)

Maughan, B. J., Giles, P. A., Rines, K. J., et al. 2016, *MNRAS*, 461, 4182, doi: [10.1093/mnras/stw1610](https://doi.org/10.1093/mnras/stw1610)

Maughan, B. J., Jones, C., Forman, W., & Van Speybroeck, L. 2008, *ApJS*, 174, 117, doi: [10.1086/521225](https://doi.org/10.1086/521225)

Murphy, B., Yurchak, R., & Müller, S. 2024, GeoStat-Framework/PyKrig: v1.7.2, Zenodo, doi: [10.5281/ZENODO.11360184](https://doi.org/10.5281/ZENODO.11360184)

Nagai, D., Vikhlinin, A., & Kravtsov, A. V. 2007, *ApJ*, 655, 98, doi: [10.1086/509868](https://doi.org/10.1086/509868)

Nelson, K., Lau, E. T., & Nagai, D. 2014, *ApJ*, 792, 25, doi: [10.1088/0004-637X/792/1/25](https://doi.org/10.1088/0004-637X/792/1/25)

Nelson, K., Rudd, D. H., Shaw, L., & Nagai, D. 2012, *ApJ*, 751, 121, doi: [10.1088/0004-637X/751/2/121](https://doi.org/10.1088/0004-637X/751/2/121)

Overzier, R. A. 2016, *A&A Rv*, 24, 14, doi: [10.1007/s00159-016-0100-3](https://doi.org/10.1007/s00159-016-0100-3)

Parekh, V., van der Heyden, K., Ferrari, C., Angus, G., & Holwerda, B. 2015, *A&A*, 575, A127, doi: [10.1051/0004-6361/201424123](https://doi.org/10.1051/0004-6361/201424123)

Plionis, M., Barrow, J. D., & Frenk, C. S. 1991, *MNRAS*, 249, 662, doi: [10.1093/mnras/249.4.662](https://doi.org/10.1093/mnras/249.4.662)

Poole, G. B., Fardal, M. A., Babul, A., et al. 2006, *MNRAS*, 373, 881, doi: [10.1111/j.1365-2966.2006.10916.x](https://doi.org/10.1111/j.1365-2966.2006.10916.x)

Popesso, P., Biviano, A., Marini, I., et al. 2024, arXiv e-prints, arXiv:2411.16555, doi: [10.48550/arXiv.2411.16555](https://doi.org/10.48550/arXiv.2411.16555)

Press, W. H., & Schechter, P. 1974, *ApJ*, 187, 425, doi: [10.1086/152650](https://doi.org/10.1086/152650)

Rasia, E., Tormen, G., & Moscardini, L. 2004, *MNRAS*, 351, 237, doi: [10.1111/j.1365-2966.2004.07775.x](https://doi.org/10.1111/j.1365-2966.2004.07775.x)

Rasia, E., Ettori, S., Moscardini, L., et al. 2006, *MNRAS*, 369, 2013, doi: [10.1111/j.1365-2966.2006.10466.x](https://doi.org/10.1111/j.1365-2966.2006.10466.x)

Russell, H. R., Lopez, L. A., Allen, S. W., et al. 2024, *Universe*, 10, 273, doi: [10.3390/universe10070273](https://doi.org/10.3390/universe10070273)

Sanders, J. S., & Fabian, A. C. 2001, *MNRAS*, 325, 178, doi: [10.1046/j.1365-8711.2001.04410.x](https://doi.org/10.1046/j.1365-8711.2001.04410.x)

Sasaki, S. 1996, *PASJ*, 48, L119, doi: [10.1093/pasj/48.6.L119](https://doi.org/10.1093/pasj/48.6.L119)

Shin, J., Woo, J.-H., & Mulchaey, J. S. 2016, *ApJS*, 227, 31, doi: [10.3847/1538-4365/227/2/31](https://doi.org/10.3847/1538-4365/227/2/31)

Tozzi, P., & Norman, C. 2001, *ApJ*, 546, 63, doi: [10.1086/318237](https://doi.org/10.1086/318237)

Vikhlinin, A., Kravtsov, A., Forman, W., et al. 2006, *ApJ*, 640, 691, doi: [10.1086/500288](https://doi.org/10.1086/500288)

Voit, G. M., Donahue, M., Bryan, G. L., & McDonald, M. 2015, *Nature*, 519, 203, doi: [10.1038/nature14167](https://doi.org/10.1038/nature14167)

Voit, G. M., Kay, S. T., & Bryan, G. L. 2005, *MNRAS*, 364, 909, doi: [10.1111/j.1365-2966.2005.09621.x](https://doi.org/10.1111/j.1365-2966.2005.09621.x)

Voit, G. M., Meece, G., Li, Y., et al. 2017, *ApJ*, 845, 80, doi: [10.3847/1538-4357/aa7d04](https://doi.org/10.3847/1538-4357/aa7d04)

von der Linden, A., Mantz, A., Allen, S. W., et al. 2014, *MNRAS*, 443, 1973, doi: [10.1093/mnras/stu1423](https://doi.org/10.1093/mnras/stu1423)

White, S. D. M., Navarro, J. F., Evrard, A. E., & Frenk, C. S. 1993, *Nature*, 366, 429, doi: [10.1038/366429a0](https://doi.org/10.1038/366429a0)

Wright, E. L. 2006, *PASP*, 118, 1711, doi: [10.1086/510102](https://doi.org/10.1086/510102)

Yuan, Z. S., & Han, J. L. 2020, *Monthly Notices of the Royal Astronomical Society*, 497, 5485, doi: [10.1093/mnras/staa2363](https://doi.org/10.1093/mnras/staa2363)

Yuan, Z. S., Han, J. L., & Wen, Z. L. 2022, *MNRAS*, 513, 3013, doi: [10.1093/mnras/stac1037](https://doi.org/10.1093/mnras/stac1037)

Zenteno, A., Hernández-Lang, D., Klein, M., et al. 2020, *MNRAS*, 495, 705, doi: [10.1093/mnras/staa1157](https://doi.org/10.1093/mnras/staa1157)

ZuHone, J. A., Markevitch, M., & Lee, D. 2011, *ApJ*, 743, 16, doi: [10.1088/0004-637X/743/1/16](https://doi.org/10.1088/0004-637X/743/1/16)

ZuHone, J. A., Markevitch, M., Ruszkowski, M., & Lee, D. 2013, *ApJ*, 762, 69, doi: [10.1088/0004-637X/762/2/69](https://doi.org/10.1088/0004-637X/762/2/69)